Interplay between charge ordering and geometric ferroelectricity in $LuFe_2O_4/LuFeO_3$ superlattices

Menglei Li,[1,*] Shaobo Cheng,[2,†] Wenbin Wang,[3] Xing Li,[4] Na Wang,[5] and Yimei Zhu[2]

[1]*Department of Physics, Capital Normal University, Beijing 100048, People's Republic of China*

[2]*Department of Condensed Matter Physics and Materials Science, Brookhaven National Laboratory, Upton, New York 11973, USA*

[3]*Institute for Nanoelectronics Devices and Quantum Computing, Fudan University, Shanghai 200433, People's Republic of China*

[4]*Key Laboratory of Material Physics, Ministry of Education, School of Physics and Microelectronics, Zhengzhou University, Zhengzhou 450052, People's Republic of China*

[5]*Department of Physical Chemistry, University of Science and Technology Beijing, Beijing 100083, People's Republic of China*

(Received 19 January 2021; revised 20 July 2021; accepted 13 September 2021; published 27 September 2021)

Oxide superlattices have drawn great attention owing to the intriguing coupling among elastic, electrical, and magnetic orderings at the interfaces and the emergence of improper ferroelectricity. Here, superlattices composed of hexagonal $LuFeO_3$ (h-$LuFeO_3$) and $LuFe_2O_4$ are investigated via density functional theory calculations. h-$LuFeO_3$ is a well-known multiferroic material that is stable only in thin film or doped bulk state, while $LuFe_2O_4$ is a charge ordered (CO) material where the existence of ferroelectricity is still a controversy. We have found that the CO-induced polarizations in $LuFe_2O_4$ layers coexist with the geometric polarizations in h-$LuFeO_3$ layers in the $(LuFe_2O_4)_m/(LuFeO_3)_n$ superlattices with different periodicities, and the ferroelectric states are generally preferred over the antiferroelectric states for $LuFe_2O_4$ in superlattices. The out-of-plane polarizations in h-$LuFeO_3$ and $LuFe_2O_4$ layers tend to be aligned in parallel, and the overall polarization increases with the ratio of h-$LuFeO_3$. The influence of layered polarizations on the local electrostatic potential is not significant except the detected small trend caused by the CO-induced polarization within a FeO bilayer. Additionally, the local electronic structures show that the Fermi level position in a certain layer can be tuned by the valences of Fe in this layer and the polarization distributions in neighboring layers. $LuFe_2O_4$ layers sandwiched between thick h-$LuFeO_3$ layers are more susceptible. The calculated configurations of the superlattices are supported by atomic-resolution transmission electron microscopy experiments. Our results pave the way for tunable ferroelectricity in superlattice systems and create a playground for manipulating the coupling between various degrees of freedom.

DOI: 10.1103/PhysRevMaterials.5.094412

I. INTRODUCTION

$LuFe_2O_4$, a typical rare earth ferrite with charge ordering (CO) of Fe^{2+}/Fe^{3+} ions, has attracted intense research attention. The CO not only strongly couples with spin degrees of freedom but also possibly induces ferroelectric order and realizes multiferroicity in $LuFe_2O_4$ [1,2]. It is proposed that the arrangement of Fe^{2+} and Fe^{3+} ions leads to polar FeO bilayers and consequently a sizeable polarization. However, experiments on $LuFe_2O_4$ yield contradictive results [3,4]. Angst *et al.* [3] suggested that polar bilayers have antiferroelectric stacking, while Groot *et al.* [4] showed that FeO bilayers are charged but nonpolar based on single-crystal x-ray diffraction data. Currently, it is commonly accepted among experimentalists that remnant polarization measured in pyroelectric current experiments is caused by external effects, and ferroelectricity cannot arise from CO in pristine $LuFe_2O_4$, excluding this ferrite from the multiferroic family with both ferroelectricity and magnetism [5]. Fortunately, superlattice modulation as well as interface engineering are effective ways to introduce favorable multiferroic properties into complex oxides, such as improper ferroelectricity in perovskite superlattices and large polarization and strong magnetoelectric coupling in hexagonal manganite superlattices [6–9]. It is natural to consider hexagonal $LuFeO_3$ (h-$LuFeO_3$) for the construction of a superlattice with $LuFe_2O_4$. h-$LuFeO_3$ is a geometric ferroelectric material, like $YMnO_3$, but has weak ferromagnetism $<\sim 150\,K$ [9–12]. It can only be stabilized in a thin film form or the bulk state with chemical dopants at Lu/Fe sites, which limits its applications [13,14]. Since h-$LuFeO_3$ has the same chemical elements and a well-matched lattice structure with $LuFe_2O_4$, stable $LuFe_2O_4/LuFeO_3$ superlattices can be realized based on previous studies [6,7,15]. Additionally, emergent multiferroic properties may be expected in $LuFe_2O_4/LuFeO_3$ superlattices.

Previous works are lacking of systematic investigations on the detailed physical mechanism of $(LuFe_2O_4)_m/(LuFeO_3)_n$ superlattices with a wide range of periodicities, where m and n are integers and > 1 with different m/n ratios. Additionally, since Fe ions in $LuFe_2O_4$ and h-$LuFeO_3$ have different valence states, the charge redistribution around the $LuFe_2O_4/LuFeO_3$ interface is also essential but has never been reported. Hence, we have studied the $(LuFe_2O_4)_m/(LuFeO_3)_n$ superlattices, where $m, n = 1, \ldots, 3$, aiming to achieve a comprehensive understanding of the ferroelectricity and CO mediated by the periodicity of the superlattice and the coupling between these two or-

*Corresponding author: limenglei@cnu.edu.cn

†Corresponding author: shcheng@bnl.gov

derings at the interfaces. By density functional theory (DFT) calculations, we found that the most stable states of the superlattices under investigation are all ferroelectric, and the CO in the $LuFe_2O_4$ layers can induce polarizations that tend to align with the polarizations of h-$LuFeO_3$ layers. The overall polarization increases with increasing h-$LuFeO_3$ layers since the ferroelectricity in h-$LuFeO_3$ layers is more robust. The local electrostatic potential and local electronic structure in individual layers of the superlattices altered by the local polarization were also investigated, showing that the influence of superlattice polarization distribution on the local electronic properties is limited except for the small $LuFe_2O_4$ layers between large regions of h-$LuFeO_3$ layers with opposite polarizations. All these $(LuFe_2O_4)_m/(LuFeO_3)_n$ superlattice configurations were further supported by our transmission electron microscopy (TEM) observations.

II. CONSTRUCTION OF THE SUPERLATTICES

The atomic structures of the unit cells of $LuFe_2O_4$ without the consideration of CO and h-$LuFeO_3$ in the high-symmetry paraelectric phase are shown in Fig. 1, viewing along the [100] zone axis. The hexagonal unit cells of $LuFe_2O_4$ and paraelectric h-$LuFeO_3$ have similar in-plane lattice parameters. As shown in Fig. 1(a), a unit cell of $LuFe_2O_4$ contains three alternatively arranged FeO bilayers and Lu layers. For convenience, we denote the FeO bilayer with the Lu layer ($\frac{1}{3}c$ of $LuFe_2O_4$ unit cell) as the $LuFe_2O_4$ block. Similarly, a unit cell of h-$LuFeO_3$ consists of two different FeO single layers and two Lu layers, as shown in Fig. 1(b). Thus, we define $\frac{1}{2}c$ of h-$LuFeO_3$ as one h-$LuFeO_3$ block. Different from h-$LuFeO_3$, a mirror reflection about the (001) plane alters the arrangement of $LuFe_2O_4$ blocks, as shown in the right panel of Fig. 1(a), which is inequivalent to the original lattice. When $LuFe_2O_4$ blocks are stacked with odd-numbered h-$LuFeO_3$ blocks, $LuFe_2O_4$ blocks are "reflected" by h-$LuFeO_3$ h-$LuFeO_3$ and need to be reflected back to satisfy the periodic boundary conditions; therefore, the total number of the blocks should be doubled along the [001] direction (c axis), as in the cases of $(LuFe_2O_4)_1/(LuFeO_3)_1/(LuFe_2O_4)_1/(LuFeO_3)_1$ (1111), $(LuFe_2O_4)_2/(LuFeO_3)_1/(LuFe_2O_4)_2/(LuFeO_3)_1$ (2121), $(LuFe_2O_4)_3/(LuFeO_3)_1/(LuFe_2O_4)_3/(LuFeO_3)_1$ (3131), $(LuFe_2O_4)_1/(LuFeO_3)_3/(LuFe_2O_4)_1/(LuFeO_3)_3$ (1313), and $(LuFe_2O_4)_2/(LuFeO_3)_3/(LuFe_2O_4)_2/(LuFeO_3)_3$ (2323). We use $m_1n_1m_2n_2$ as the abbreviated representation, where m_1 and m_2 represent the numbers of $LuFe_2O_4$ blocks in the lower $LuFe_2O_4$ layer and upper $LuFe_2O_4$ layer, $n1$ and $n2$ represent the numbers of h-$LuFeO_3$ blocks in the lower h-$LuFeO_3$ layer and upper h-$LuFeO_3$ layer in the constructed superlattices, as shown in Fig. 2. When $LuFe_2O_4$ blocks meet with even-numbered h-$LuFeO_3$ blocks, h-$LuFeO_3$ will not influence the arrangement of the $LuFe_2O_4$ blocks, and the $LuFe_2O_4$ blocks are stacked as if there were no h-$LuFeO_3$ layer. However, the total numbers of the $LuFe_2O_4$ blocks must be an integral multiple of 3. With these principles, we construct $(LuFe_2O_4)_2/(LuFeO_3)_2/(LuFe_2O_4)_1/(LuFeO_3)_2$ (2212) and $(LuFe_2O_4)_3/(LuFeO_3)_2/(LuFe_2O_4)_3/(LuFeO_3)_2$ (3232) superlattices. Due to the large numbers of atoms and huge dimensions along the out-of-plane direction, we investigated the seven smallest superlattices considering the computation cost, and the conclusions are quite consistent and can be generalized to other configurations. All investigated superlattices are shown in Figs. 1(c)–1(i).

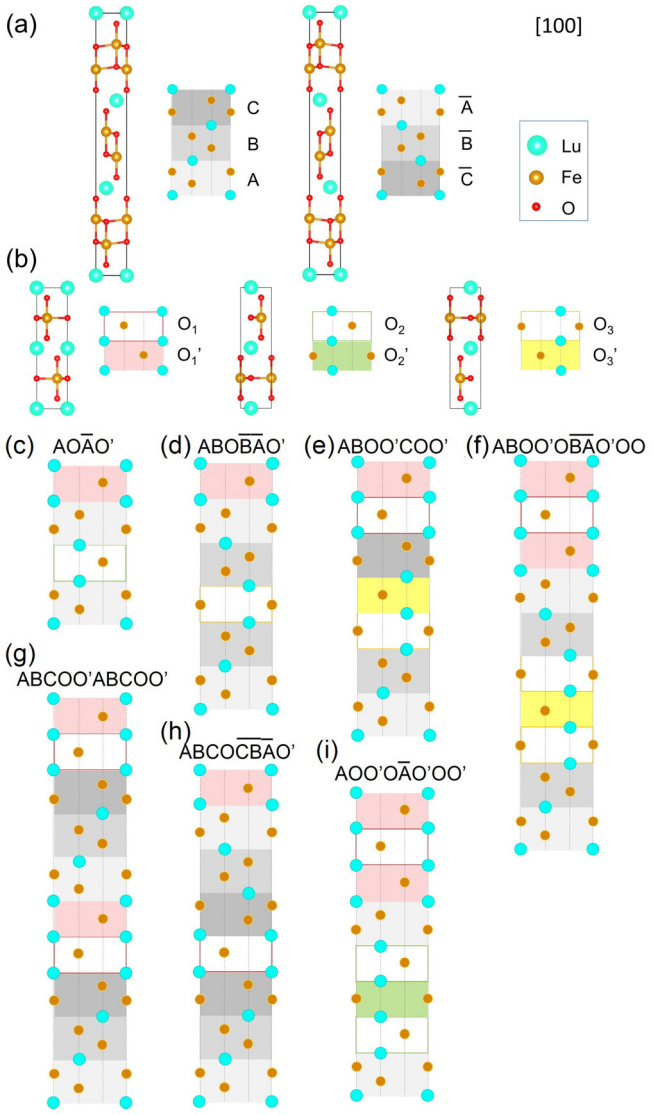

FIG. 1. (a) Atomic structure and sketch of each block for the $LuFe_2O_4$ unit cell viewed along the [100] zone axis. The three blocks in a unit cell are labeled with A, B, and C with different gray levels. When the mirror reflection through the (001) plane is performed for $LuFe_2O_4$, the arrangement of the three blocks is reversed, as $\bar{C}$, $\bar{B}$, and $\bar{A}$. (b) Atomic structure and sketch of each block for the h-$LuFeO_3$ paraelectric unit cell, denoted with O and O′. The unit cell center has different choices in which the coordinates of the atoms are different. According to the in-plane positions of Fe ions in the unit cell, the h-$LuFeO_3$ blocks are sorted as O_1, O_2, and O_3 plot with different colors, which are the same in nature. Using certain $LuFe_2O_4$ blocks and h-$LuFeO_3$ blocks, the superlattices (c) 1111, (d) 2121, (e) 2212, (f) 2323, (g) 3232, (h) 3131, and (i) (1313) are built, which are the seven smallest and typical superlattices. Note that the choices of $LuFe_2O_4$ and h-$LuFeO_3$ blocks must be matched and satisfy the out-of-plane stacking rule. Big cyan spheres and solid cyan circles both represent Lu ions, medium golden spheres and solid golden circles both represent Fe ions, and small red ions represent O ions which have been omitted in the block sketches.

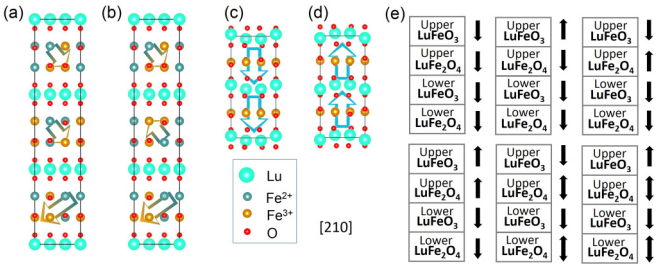

FIG. 2. (a) Charge ordered (CO) unit cell of $LuFe_2O_4$ with CO-induced ferroelectricity. (b) CO unit cell of $LuFe_2O_4$ with CO-induced antiferroelectricity. (c) Ferroelectric h-$LuFeO_3$ unit cell with downward polarization. (d) Ferroelectric h-$LuFeO_3$ unit cell with upward polarization. Here, different colors of Fe ions represent different valences, and hollow arrows represent the polarization directions of the corresponding $LuFe_2O_4$ or h-$LuFeO_3$ blocks. (e) Six types of polarization arrangements for a certain $m_1n_1m_2n_2$ superlattice. To be specific, the lower (upper) $LuFe_2O_4$ layer contains $m1$ ($m2$) $LuFe_2O_4$ blocks, and the lower (upper) h-$LuFeO_3$ layer contains $n1$ ($n2$) h-$LuFeO_3$ blocks. Black arrows aside the $LuFe_2O_4$ or h-$LuFeO_3$ blocks represent the polarization direction along the c axis of the layers. The ↕ arrow indicates that the $LuFe_2O_4$ layer is antiferroelectric.

To study the CO $LuFe_2O_4$ and ferroelectric h-$LuFeO_3$, both materials must be triply enlarged with the new a axis rotating 30° from the original one. The lengths of the new in-plane vectors are $\sqrt{3}$ times of those of the original ones. Figures 2(a)–2(d) show the enlarged unit cells along the original [210] zone axis, in which the atom numbers are tripled. In $LuFe_2O_4$ layers, we set the CO proposed by Xiang and Wangbo [1], which leads to a polar bilayer, as shown in Fig. S1 in the Supplemental Material [16]. Specifically, there are equal numbers of Fe^{2+} and Fe^{3+} ions in a FeO bilayer, with an Fe^{2+}/Fe^{3+} ratio of 2:1 in one sublayer but 1:2 in the other. The polarization within a bilayer has a certain angle from the c axis. The ferroelectric and antiferroelectric states of $LuFe_2O_4$ are shown in Figs. 2(a) and 2(b). In h-$LuFeO_3$ layers, all Fe ions initially have a valence of +3 as in bulk h-$LuFeO_3$. The rumpling of Lu layers that $\frac{1}{3}$ of Lu ions move oppositely along the c axis against the left $\frac{2}{3}$ Lu ions leads to the polarization along the c axis, as shown in Figs. 2(c) and 2(d).

Figure 2(e) illustrates six representative types of polarization arrangements in the superlattices, which are represented by ↓↓↓↓, ↓↓↓↑, ↓↓↑↓, ↓↓↑↑, ↕↓↕↓, and ↕↓↕↑. The first and third arrows represent the c-component polarization directions of the lower and upper $LuFe_2O_4$ layers, and the second and fourth arrows represent the polarization directions of the lower and upper h-$LuFeO_3$ layers. A ↓ (↑) symbol visually represents the downward (upward) polarization of the corresponding layer, and a ↕ symbol represents that the $LuFe_2O_4$ layer is antiferroelectric.

III. THEORETICAL RESULTS ON DIFFERENT SUPERLATTICES

As mentioned in Sec. II, seven types of superlattices with different periodicities were investigated using DFT calculations. The DFT-based generalized gradient approximation (GGA) exchange-correlation functional is known to underestimate the band gaps of insulating and semiconductive systems, while the hybrid exchange correlation functionals such as B3LYP or B3PW, could give better agreement with experiments regarding the related ferroelectric materials of an ABO_3 perovskite [17,18], whereas we still used the GGA functional plus U correction to match the experiments since the adoption of hybrid exchange correlation functionals is quite costly for large systems such as the superlattices. For each superlattice, four to six different polarization arrangements were set as the initial state. We mainly focus on resolving the following questions: What is the final polarization state for each superlattice, and what is the universal law? How does the geometric ferroelectricity of h-$LuFeO_3$ layers interplay with the CO of $LuFe_2O_4$ layers? Can the polarization distribution and CO across the superlattices be used to modulate the electronic properties of the layers? Through theoretical studies, we will answer the above questions.

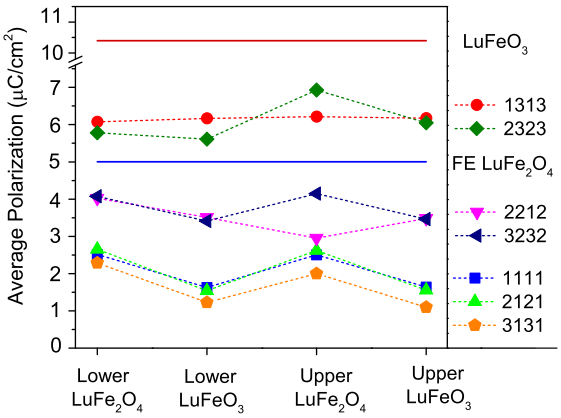

FIG. 3. The relaxed average polarizations for the lower $LuFe_2O_4$ layers, lower h-$LuFeO_3$ layers, upper $LuFe_2O_4$ layers, and upper h-$LuFeO_3$ layers in the seven superlattices with all the polarizations initially pointing down (↓↓↓↓).

A. Superlattices with aligned polarizations

We first set the polarizations of the $LuFe_2O_4$ and h-$LuFeO_3$ layers along the c axis all pointing down. The calculated local polarizations after relaxation are shown in Tables S1–S7 in the Supplemental Material [16]. The averaged polarizations of the lower $LuFe_2O_4$, lower h-$LuFeO_3$, upper $LuFe_2O_4$ and upper h-$LuFeO_3$ layers are shown in Fig. 3. The bulk polarizations of h-$LuFeO_3$ and $LuFe_2O_4$ in the ferroelectric state are also shown for reference. We note that these seven polarization lines can be divided into three groups according to the number of h-$LuFeO_3$ blocks (n). Since the bulk polarization of $LuFe_2O_4$ is weaker than that of h-$LuFeO_3$, more h-$LuFeO_3$ blocks should lead to a stronger overall polarization of the superlattice. However, our results show that most of polarizations of superlattices are smaller than that of bulk $LuFe_2O_4$ in the ferroelectric state. Bulk $LuFe_2O_4$ in the ferroelectric state is less stable than the antiferroelectric state by 5 meV/f.u. from our calculations, and recent experiments also show no detectable polarization in $LuFe_2O_4$ [1,3]. At this point, we are unable to compare the ferroelectricity of $LuFe_2O_4/LuFeO_3$ superlattices with bulk antiferroelectric state of $LuFe_2O_4$.

TABLE I. The formation energies (in units of eV) and interface energies (in units of mJ m^{-2}) for the seven superlattices in their most stable polarization arrangements after structural and charge relaxations. Note that the initial polarization arrangements and the polarization arrangements after relaxations are both listed in the table.

	1111	2121	3131	1313	2323	2212	3232
Initial polarization arrangement	↓↓↓↑	↓↓↓↑	↕↓↕↓	↓↓↑↑	↓↓↓↑	↕↓↕↑	↕↓↕↑
Final polarization arrangement	↓↓↓↓	↓↓↓↓	↕↓↕↓	↑↑↑↑	↓↓↓↓	↓↓↓↓	↕↓↕↓
Formation energy	0.103	−0.236	−0.164	−0.301	0.289	−0.484	−0.634
Interface energy	13.6	−30.7	−21.3	−39.2	37.6	−63.0	−82.5

Therefore, superlattices with antiferroelectric $LuFe_2O_4$ and oppositely aligned polarizations have been set and free to relax to see whether the ferroelectric state or the antiferroelectric state is more stable in the superlattices under the influence of the interfaces.

B. The most stable polarization arrangements

For the superlattices 1111 and 1313, since there is only one $LuFe_2O_4$ block in a period and antiferroelectric $LuFe_2O_4$ layers cannot be set, four initial polarization arrangements ↓↓↓↓, ↓↓↓↑, ↓↓↑↓, and ↓↓↑↑ are considered in total. Meanwhile, for the superlattice 2212, ↕↓↕↓ and ↓↓↑↓ are equivalent, and so are the polarization arrangements ↕↓↕↑ and ↓↓↑↑; hence, there are also only four initial arrangements. For the four remaining superlattices, the six polarization arrangements shown in Fig. 2(e) are all set as the initial states. Then the ionic positions and the charges of Fe ions are free to relax. We select the final state with the lowest energy for each superlattice and calculate the formation energy using $E^{\text{form}} = E^{m_1n_1m_2n_2} - \frac{m_1+m_2}{3}E^{\text{LuFe}_2\text{O}_4} - \frac{(n_1+n_2)}{2}E^{\text{h-LuFeO}_3}$, where $E^{m_1n_1m_2n_2}$ is the total energy of the superlattice $m_1n_1m_2n_2$, m_1+m_2 is the total number of the $LuFe_2O_4$ blocks, n_1+n_2 is the total number of the h-$LuFeO_3$ blocks, $E^{\text{LuFe}_2\text{O}_4}$ is the energy of a $LuFe_2O_4$ unit cell in the CO phase, and $E^{\text{h-LuFeO}_3}$ is the energy of a h-$LuFeO_3$ unit cell in the ferroelectric phase. Furthermore, the interface energy between h-$LuFeO_3$ and $LuFe_2O_4$ layers is calculated through dividing the formation energy by 4, as there are four interfaces. Calculated formation energies and interface energies are shown in Table I. Most of the formation energies are negative and very small, indicating that the superlattices can form easily. Like the formation energies, most of the interface energies are negative except those of 1111 and 2323 superlattices. The interface energies have the same magnetic order as neutral domain walls in ferroelectrics such as $YMnO_3$ [19] and $BaTiO_3$ [20] but much smaller than those of charged ferroelectric domain walls [21].

After the structural relaxation with the relaxation of CO, the final polarization states have changed. The relaxed local polarizations for all the considered polarization arrangements of the seven superlattices can be found in Tables S1–S7 in the Supplemental Material [16]. Additionally, for each superlattice, the calculated energies of the polarization arrangements compared with the most stable ones are listed in Table S8 in the Supplemental Material [16]. We find one common result for the most stable polarization distributions of all the superlattices: polarizations in $LuFe_2O_4$ and h-$LuFeO_3$ blocks tend to align in the same direction, as shown in Fig. 4. For 3131, 2212, and 3232 superlattices, which have the initial setting of antiferroelectric $LuFe_2O_4$ layers, the relaxed local polarizations projected to the c axis are influenced by the polarizations of h-$LuFeO_3$ layers, and the downward polarizations are much stronger than the upward polarizations. For 1111 and 2121 superlattices, the lower and upper layers of h-$LuFeO_3$ initially have opposite polarizations (↓↓↓↑). After relaxations, the polarizations are all pointing down. For the 1313 and 2323 superlattices, the local polarizations are totally dominated by the polarizations of h-$LuFeO_3$ blocks and show perfect ferroelectric arrangements. Additionally, local polarizations of the 1313 superlattice naturally relax to

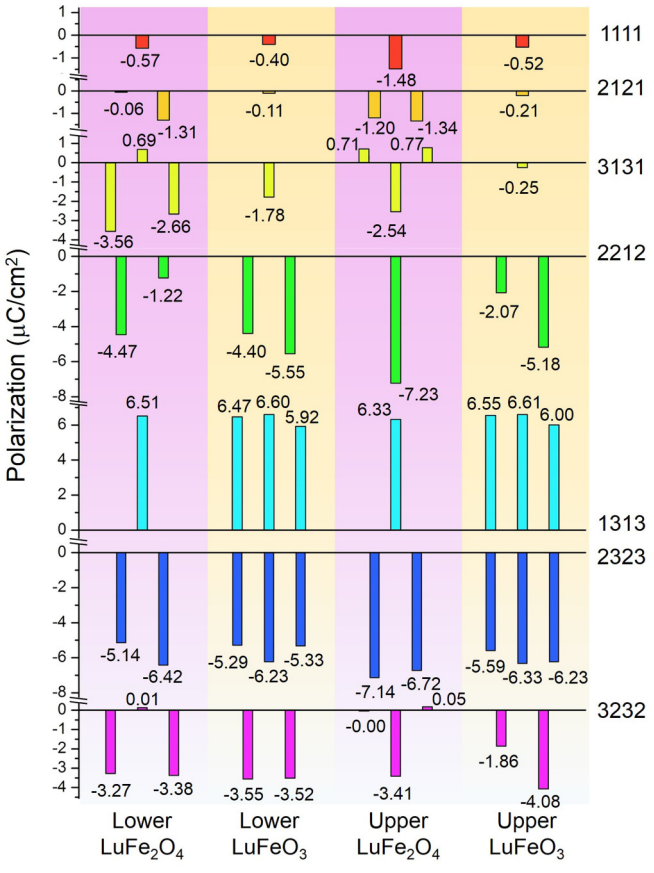

FIG. 4. Local polarizations of all the blocks in the lower $LuFe_2O_4$, lower $LuFeO_3$, upper $LuFe_2O_4$, and upper $LuFeO_3$ layers for the seven considered superlattices in their most stable final states. The periodicities of the superlattices are labeled in the right of the horizontal axes. The exact values of the polarizations are marked at the end of the bars representing the block polarizations in units of μC cm^{-2}.

the upward direction since, for h-$LuFeO_3$, the upward and downward polarizations are equivalent, and the polarizations of minor $LuFe_2O_4$ blocks compromise with those of the majority blocks of h-$LuFeO_3$. It also can be found that the more h-$LuFeO_3$ blocks, the larger the overall polarization. To summarize, the overall ferroelectric state is more stable than the antiferroelectric state in superlattices, indicating an enhanced ferroelectricity in $LuFe_2O_4$/$LuFeO_3$ superlattices.

C. Local electrostatic potential induced by polarizations

In the superlattices, local polarizations induce a depolarization field, and thus, electrons in different layers have different electrostatic potentials. However, the depolarization field cannot keep increasing; otherwise, polar catastrophe, i.e., the divergence of the electrostatic potential at macroscale, would occur. The periodic boundary conditions in our simulations impose short-circuit electrical conditions throughout the superlattices in the out-of-plane direction, which naturally prevents the system from electrostatic catastrophe.

Here, the planar-averaged electrostatic potentials for electrons as a function of the c coordinate along with the local polarizations for several typical superlattices are calculated and shown in Fig. 5. The potential curves are oscillated: At the FeO planes or the Lu planes where there are more positive charges, the electrostatic potentials are negative and have local minima; between two local minima, the potential reaches a positive local maximum. Local potentials at FeO planes are significantly lower than those at Lu planes. It is hard to tell the overall trend of the electrostatic potential since periodic boundary conditions are imposed, but there are some details that reflect the connections with local polarization and CO. First, for the FeO single layer in h-$LuFeO_3$ layers, the maximal and minimal electrostatic potentials are both lower than those for the FeO bilayers in $LuFe_2O_4$ layers, which is simply because cations are less dense in h-$LuFeO_3$ layers. Second, within a FeO bilayer, the electrostatic potential of the FeO sublayer below is lower than that of the upper FeO sublayer if the polarization of this bilayer is large and negative (pointing down). Meanwhile, if the polarization is positive (pointing up) or negative with sufficiently small magnitude, the lower FeO sublayer will have higher electrostatic potential. It can be understood in two aspects. One is from the depolarization field, which is opposite to the polarization direction, as sketched in Fig. 6(a). The electrostatic potential becomes low at high depolarization field. On the other aspect, the FeO sublayer possessing more Fe^{2+} ions has higher electrostatic potential than the FeO sublayer with more Fe^{3+} ions, while CO-induced polarization points from former to the latter, which is schematically plotted in Fig. 6(b). When the CO-induced polarization and displacive polarization nearly cancel and the final polarization reverses, as the case of 2212 in Fig. 5(g), the electrostatic potential is still lower in the FeO plane with more Fe^{3+} ions and higher in the FeO plane with more Fe^{2+} ions.

The macroscopic-averaged electrostatic potentials are also plotted with VASPKIT in Fig. 5 with red lines [22]. The electrostatic potentials are averaged over 2.92 Å, which is the distance between Fe and adjacent O planes along the c axis. Only small ups and downs emerge in the macroscopic-averaged electrostatic potentials, corresponding to the energy shifts of the local densities of states (DOS). However, the overall electrostatic potential is quite flat, and thus, it can be expected that the electronic structures have no obvious shift from the bottom layer to the top layer in the superlattice systems either. Still, the difference between h-$LuFeO_3$ and $LuFe_2O_4$ layers is clearly seen from the averaged electrostatic potentials, i.e., the potential of h-$LuFeO_3$ layers is generally lower than that of $LuFe_2O_4$ layers, which introduces different energies of local electronic states between h-$LuFeO_3$ and $LuFe_2O_4$ layers.

D. Local electronic structures

The local DOS resolved to $LuFe_2O_4$ and h-$LuFeO_3$ blocks are plotted for five typical superlattice systems, as shown in Fig. 7. The total DOS and projected DOS on Fe^{3+}, Fe^{2+} $3d$ orbitals, and O $2p$ orbital are demonstrated, but DOS for electrons of Lu ions are not shown since they contribute little to the DOS near the Fermi level.

As mentioned in the last subsection, the electronic structures for most of the superlattices are only slightly influenced by local polarizations, and the total DOS display insulating nature as the bulk $LuFe_2O_4$. The valence band maximum (VBM) is composed of O $2p$ states and $3d$ states of Fe^{2+} ions, and the conduction band minimum (CBM) is composed of $3d$ states of Fe^{3+} ions. Generally, the unoccupied d states of Fe^{2+} ions (not shown in Fig. 7) have higher energies than the unoccupied d states of Fe^{3+} ions. The Fe^{3+} ion has a $3d^5$ configuration, and all d orbitals are half-occupied by single-spin electrons. In contrast, the Fe^{2+} ion has a $3d^6$ configuration. After all the d orbitals have been occupied by the electrons of the majority spin channel, the electron from the minority spin channel will fill in one $3d$ orbital, and the resultant Coulomb interaction adds to the total energy, as sketched in Fig. 7(f). As a result, in a certain layer where there are more Fe^{2+} ions, the Coulomb repulsions are stronger, and the CBM consisting of $3d$ states goes up, which leads to a broader band gap. Hence, in the h-$LuFeO_3$ layer with no Fe^{2+} ions, the unoccupied $3d$ states and thus the CBM are obviously lower than those of the $LuFe_2O_4$ layer. In this way, the position of the CBM as well as the band gap can be modulated by the ratio of Fe^{2+} to Fe^{3+} ions.

In the block-resolved local DOS, the Fermi energy is pinned so that the band bending in each block can be manifested. VBMs of $LuFe_2O_4$ blocks are closer to the Fermi level than those of h-$LuFeO_3$ blocks by 0.5 to 1 eV, which is due to the lower electrostatic potential of h-$LuFeO_3$ blocks. Compared with the local DOS resolved to the block for bulk h-$LuFeO_3$, as shown in Fig. S1 in the Supplemental Material [16], the translation of electronic states (or the shift of Fermi level) for h-$LuFeO_3$ blocks in the superlattices is also clear. Additionally, the Fermi level changes appreciably in several cases such as the h-$LuFeO_3$ layers in 1111-↓↓↑↓ superlattice [Fig. 7(b)], h-$LuFeO_3$ layers in 3131-↓↓↑↑ superlattice [Fig. 7(c)], $LuFe_2O_4$ layers in 1313-↓↓↓↑ superlattice [Fig. 7(d)], and $LuFe_2O_4$ layers in 2121-↕↓↕↑ superlattice [Fig. 7(e)]. These can all be traced to the electrostatic potentials shown in Fig. 5. For example, in the case of 1111-↓↓↑↓, the lower h-$LuFeO_3$ layer (block) has the lowest

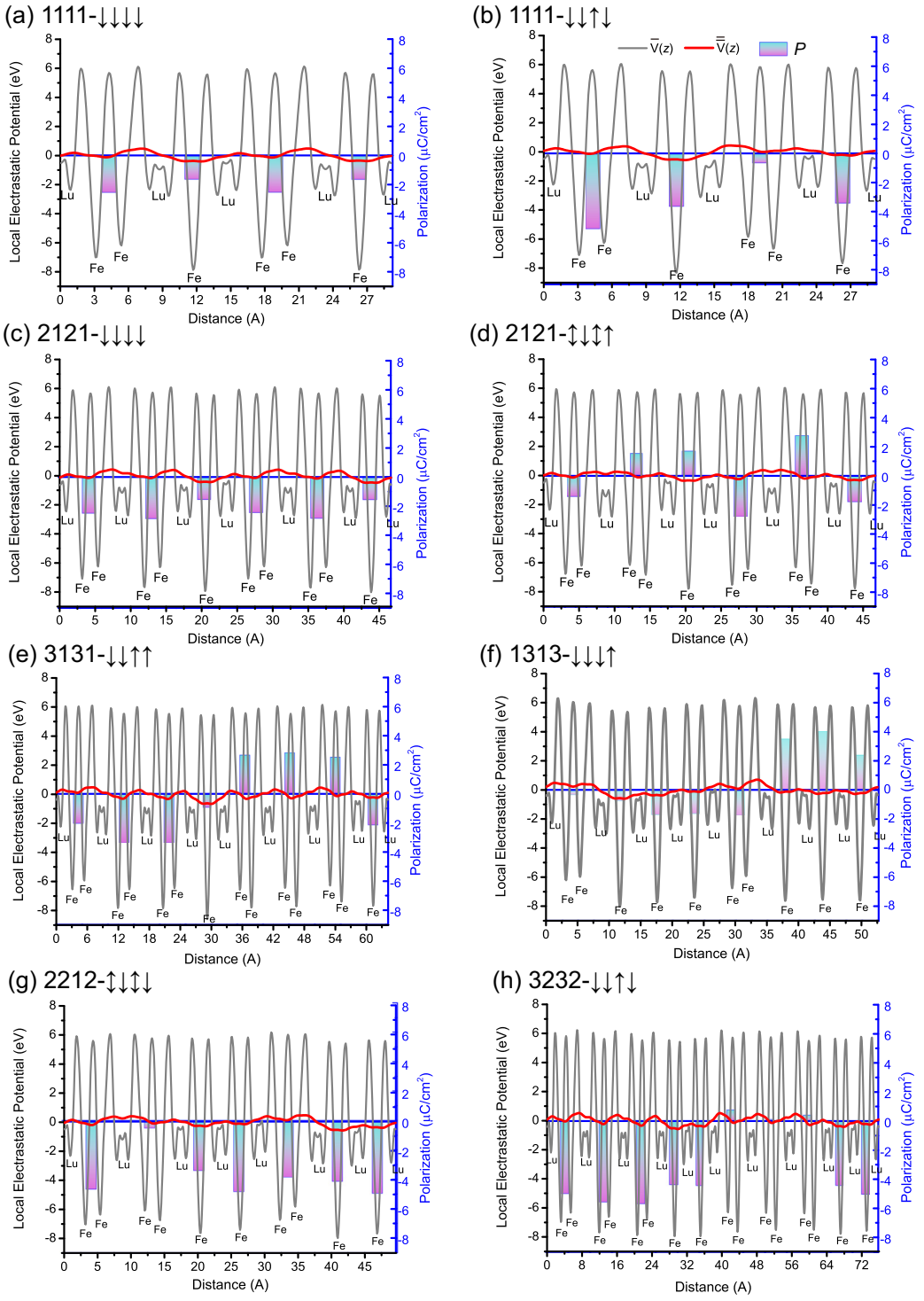

FIG. 5. Planar average electrostatic potential along the c axis (gray line) and macroscopic-averaged local electrostatic potential over 2.92 Å (read line) as functions of the distance from the bottom plane. The corresponding superlattice systems are denoted in the panels. The positions of Fe and Lu ions at the c axis are also labeled aside the potential curves. The local c components of the block-resolved polarizations are plot with blue-magenta bars overlying at the central position of each block for reference.

electrostatic potential for electrons, and thus, the DOS of the lower h-$LuFeO_3$ layer shift to the lower energies, and the Fermi energy goes up obviously. Meanwhile, the electrons in the upper h-$LuFeO_3$ layer (block) have higher electrostatic potential than those in the lower layer by ∼0.3 eV, which leads to a higher VBM of the upper h-$LuFeO_3$ closer to the Fermi energy. By the same token, in other superlattices, the Fermi level also shifts owing to the fluctuation of the local electrostatic potential.

It is interesting to compare the local electronic structures of $LuFe_2O_4$ blocks sandwiched between large regions of h-$LuFeO_3$ with opposite polarizations to those of h-$LuFeO_3$

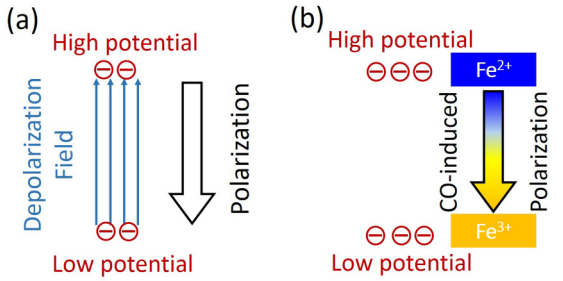

FIG. 6. Sketches of the electrostatic potential variation caused by polarization and charge ordering (CO). (a) Depolarization field induced by a sizeable polarization leads to high (low) electrostatic potential for electrons at the tail (head) of the polarization. (b) Unbalanced charges in each FeO plane of a FeO bilayer cause different electrostatic potentials for electrons. CO-induced polarization in the bilayer is represented by the arrow with gradient colors.

blocks between oppositely polarized $LuFe_2O_4$ thick layers. By considering these special cases, we can catch a glimpse of how to modulate local electronic properties with superlattice stacking. Two extreme examples, namely, 3131-↓↓↑↑ (after relaxation, the polarization arrangement transfers to ↓↓↑↓) and 1313-↓↓↓↑, are therefore addressed. The former superlattice contains $LuFe_2O_4$ layers with opposite polarization directions separated by a single h-$LuFeO_3$ block, and the latter has an individual $LuFe_2O_4$ block in the middle of head-to-head or tail-to-tail h-$LuFeO_3$ domains. From Fig. 7(c), we can see that, although the Fermi level shifts in local DOS of upper and lower h-$LuFeO_3$ blocks, it locates in the gap deeply. In contrast, local DOS for upper and lower $LuFe_2O_4$ blocks in 1313-↓↓↓↑ superlattice have substantial difference. In the lower $LuFe_2O_4$ block, which is between the head-to-head polarizations of h-$LuFeO_3$ layers, the Fermi level dips into the conduction band. Meanwhile, in the upper $LuFe_2O_4$ block between tail-to-tail polarizations, the edge of the valence band is just above the Fermi level. This feature indicates that there are charges confined at the smaller $LuFe_2O_4$ layers, just as the case of charged head-to-head/tail-to-tail domain walls in $YMnO_3$ investigated by Ref. [21]. Previous studies including Refs. [7,19] have already visited the 1313 superlattice, which was referred to as $(LuFeO_3)_3/(LuFe_2O_4)_1$. They found that the "doped type" superlattice, where there are head-to-head interfaces within h-$LuFeO_3$ layers, had electron transfer from the $LuFe_2O_4$ layer to the h-$LuFeO_3$ layer, but they did not go further on the "undoped type," which is very similar to the 1313-↓↓↓↑ superlattice. Here, we have demonstrated that the "undoped type" also has confining charges at $LuFe_2O_4$ layers.

In summary, the local position of the Fermi level in each block can be modulated in the superlattice since the depolarization field of the local polarizations alters the local electrostatic potential. The electronic properties of $LuFe_2O_4$ layers sandwiched between thick h-$LuFeO_3$ layers are more susceptible than those of h-$LuFeO_3$ layers between $LuFe_2O_4$ layers. Large h-$LuFeO_3$ regions with head-to-head or tail-to-tail polarizations can induce confined charges at the sandwiching of smaller $LuFe_2O_4$ layers. Future work will focus on the stabilization of such head-to-head/tail-to-tail polarization arrangements in the superlattices by means of electric field, strain, chemical doping, etc.

IV. EXPERIMENTAL OBSERVATION OF SUPERLATTICELIKE STRUCTURES

High-angle annular dark field STEM (HAADF-STEM) images for $LuFe_2O_4$ single crystalline samples are shown in Fig. 8, where the image contrast is sensitive to the atomic number. In Fig. 8(a), the low magnification STEM image of the sample is presented, containing several horizontal bright lines, which is magnified into a high-resolution image, as shown in Fig. 8(b). Since the atoms with brighter contrast are Lu atoms and the ones with relatively darker contrast are Fe atoms in Fig. 8(b), the different distances between the Lu layers imply that each bright line in Fig. 8(a) is composed of two h-$LuFeO_3$ blocks and several $LuFe_2O_4$ blocks between them as the constructed superlattices in DFT calculations. The brightness profile in Fig. 8(d) corresponds to the atomic layers in the white dash rectangle region in Fig. 8(b) from the top to the bottom, further illustrating the alternative stacking of h-$LuFeO_3$ blocks and $LuFe_2O_4$ blocks. Figure 8(e) shows the atomic structure acquired from the [210] zone axis of $LuFe_2O_4$, which is 30° away from the [100] zone axis, as shown in Figs. 8(b) and 8(d). Careful inspection on the HAADF-STEM images suggests that the $LuFe_2O_4$ sample is like a $LuFe_2O_4/LuFeO_3$ superlattice of $m111$, which is reconstructed in Figs 8(c) and 8(f) with VESTA [23], matching with Fig. 8(b) from the [100] zone axis and Fig. 8(e) from the [210] zone axis, respectively.

In Fig. 8, only one type of superlatticelike structure is demonstrated, whereas other types of superlatticelike structures with one to three $LuFe_2O_4$ blocks in the middle of the h-$LuFeO_3$ blocks, i.e., $m121$ and $m131$, are all frequently observed in the experiments. The high-magnification STEM images of superlatticelike structures can be found in Fig. S3 in the Supplemental Material [16]. All the interfaces between $LuFe_2O_4$ and h-$LuFeO_3$ are along the (001) plane and extend across the whole samples. It has been reported that the CO domains are of several nanometers wide at room temperature, and they would even expand at low temperature [24,25]. It is possible that similar superlatticelike structure can be found in a broader class of materials.

V. CONCLUSIONS

In summary, we constructed the superlattices of $[(LuFe_2O_4)_m/(LuFeO_3)_n]_2$ with m, $n = 1, \ldots, 3$ and performed first-principles calculations to investigate the coupling between CO-induced polarization of $LuFe_2O_4$ layers and geometric polarization of h-$LuFeO_3$ layers. We revealed that the stabilization of the antiferroelectricity in bulk $LuFe_2O_4$ is attenuated in the superlattices. Most of the optimized superlattices have the local out-of-plane polarizations aligned along the same direction, indicating an enhanced ferroelectricity in the superlattices. Additionally, more h-$LuFeO_3$ layers lead to a stronger overall polarization since the geometric ferroelectricity is robust and becomes dominant over the CO-induced polarizations with the increase of the number of h-$LuFeO_3$ layers. In most

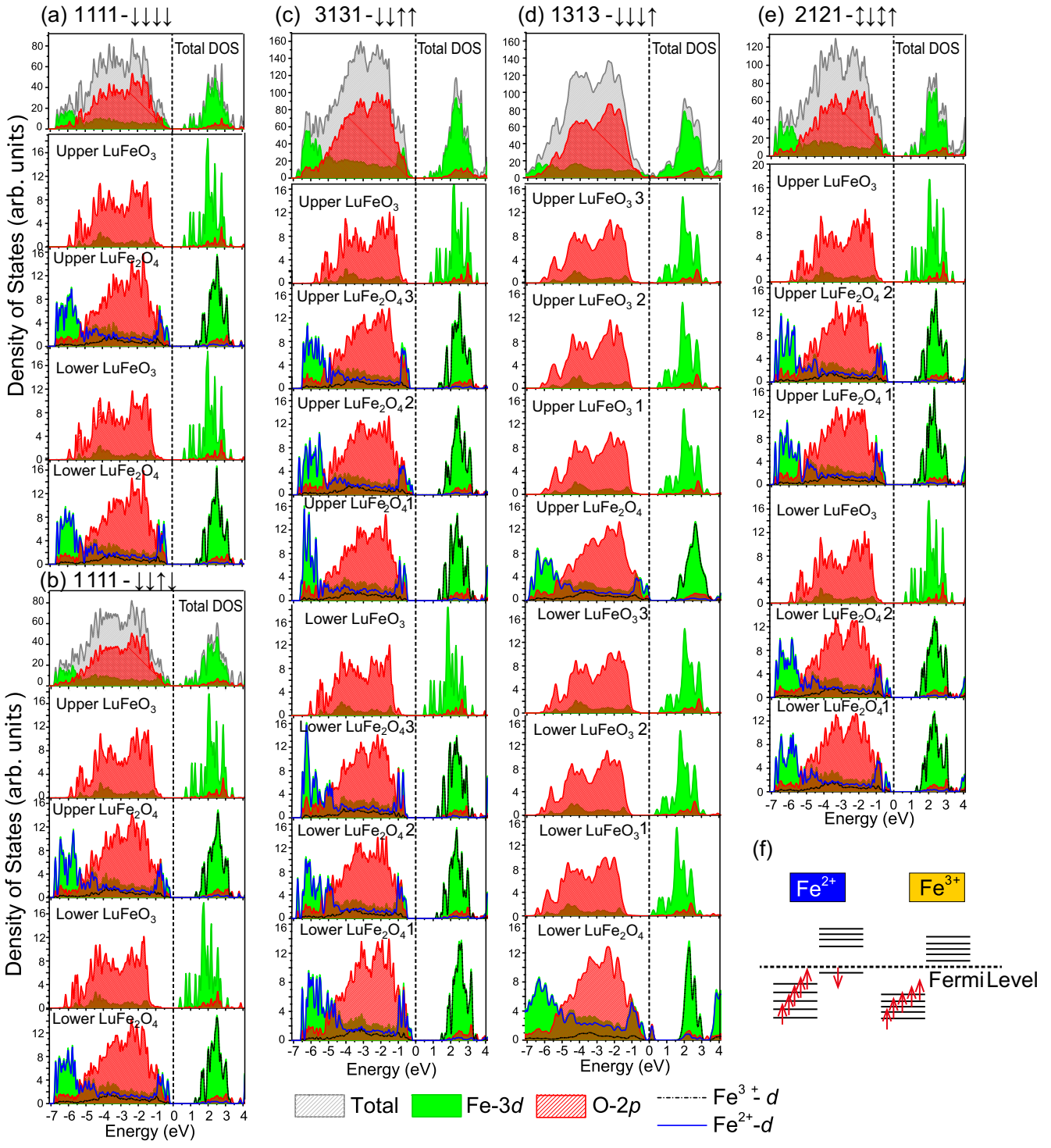

FIG. 7. (a)–(e) Total densities of states (TDOS) and projected densities of states (PDOS) on O $2p$ orbitals and Fe $3d$ orbitals. The corresponding superlattice systems are denoted in the panels. The top panels are the TDOS and PDOS for the whole superlattice structures. The local TDOS and PDOS for each block are shown below the top panels. Taking 3131-↓↓↑↑ structure for example, the eight DOS panels (except for the top one) correspond to those of the eight blocks in Fig. 1(h) in a one-by-one manner. In the h-$LuFeO_3$ layers, there are only O $2p$ states and Fe^{3+} $3d$ states; therefore, the latter are shown with green shades. In the $LuFe_2O_4$ layers, the Fe $3d$ states are divided into Fe^{3+} d states and Fe^{2+} d states. Note that the DOS from Lu atoms are not plotted here. The Fermi energy is pinned in each superlattice system and set as 0. (f) Sketch of the $3d$ orbital occupancy for Fe^{2+} and Fe^{3+} ions, respectively, where a red arrow represents a $3d$ spin-down or spin-up electron.

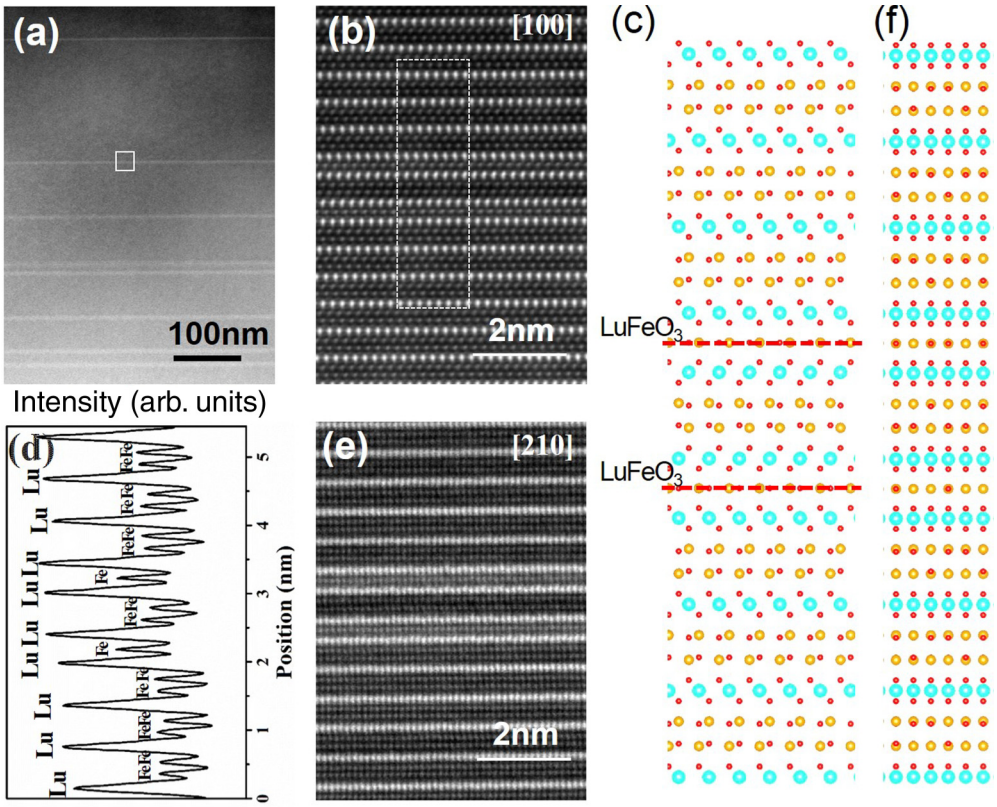

FIG. 8. (a) Low magnification high-angle annular dark field scanning transmission electron microscopy (HAADF-STEM) image of the $LuFe_2O_4$ sample. (b) The high-resolution HAADF image magnified from the white outlined rectangle region in (a). (c) The corresponding superlattice structure of the white dash rectangle region in (b). The image is viewed along the [100] zone axis. (d) The integrated intensity profile from the top to the bottom for the white dash rectangle region in (b). (e) The high-resolution HAADF image from the [210] zone axis. (f) Corresponding superlattice along the [210] zone axis. Note that, in (c) and (f), the displacements of Lu atoms are not illustrated.

cases, local polarizations only have limited influence on the layer-decomposed electronic structure, suggesting that the superlattice modulation might not be an effective method to tailor the static layered electronic properties. However, for one situation where small $LuFe_2O_4$ layers are sandwiched between large regions of h-$LuFeO_3$ layers with head-to-head/tail-to-tail polarizations, the DOS show that there are charges confined at the $LuFe_2O_4$ layers. Additionally, the positions of CBM and VBM in a certain layer can still be tuned to some extent by the Fe valences in that layer as well as the out-of-plane polarizations in the neighboring layers. Since ferrites are magnetic in nature, we also expect excellent magnetoelectric coupling properties in the $LuFe_2O_4/LuFeO_3$ superlattices, which will be the subject of future work. Lastly, these theoretically calculated superlattice structures were verified at atomic scale by HAADF-STEM experiments. Hence, our results have successfully introduced a promising superlattice system with tunable ferroelectricity.

ACKNOWLEDGMENTS

M.L. would like to thank Dr. Changsong Xu and Prof. Zhirong Liu for useful suggestions and helpful discussions. This paper was supported by the National Natural Science Foundation of China under Grants No. 12074271, No. 11804304, No. 52072345, and No. 11804021. M.L. would also like to acknowledge the support from the Beijing Municipal Commission of Education science research program General Project No. KM201810028004 and the key research project of the Academy for Multidisciplinary Studies, Capital Normal University. S.C. and Y.Z. would like to acknowledge support for the electron microscopy work at BNL from the U.S. DOS Basic Energy Sciences, Materials Sciences and Engineering Division under Contract No. DESC0012704. W.W. would like to acknowledge the National Key R&D Program of China (No. 2016YFA0300702) and the National Natural Science Foundation of China (No. 12074071). The computer simulations were carried out on the high-performance computing facility from the NSCC-TJ National Supercomputing Center, NSCC-GZ National Supercomputing Center, and Lvliang Cloud Computing Center.

APPENDIX A: FIRST-PRINCIPLES CALCULATIONS

We have performed first-principles calculations based on spin-polarized DFT as implemented in the Vienna *Ab initio* Simulation Package (VASP) [26]. The projector augmented wave pseudopotentials with the GGA of the PBEsol functional were employed. Lu $5p$, $5d$, and $6s$ electrons; Fe $3d$ and $4s$ electrons; and O $3s$ and $2p$ electrons were treated as valence electrons [27,28]. The wave functions were expanded in plane waves with an energy cutoff of 500 eV. To deal with d electrons of Fe, we have employed the GGA + U method, where

the Coulomb onsite repulsion U and the exchange parameter J were set to 7.5 and 0.95 eV, respectively. The choices of U and J were based on Refs. [1,7], both of which indicate that, for smaller values of U, the results hardly change. In all geometry optimizations, atoms were kept relaxing until the residual forces on each atom were $< 0.005\,\mathrm{eV/Å}$. Since there are at least hundreds of atoms in the superlattices, we have used a sparse Γ k-mesh of $3 \times 3 \times 1$ to sample the reciprocal space, seeking a balance between accuracy and computation cost.

The local polarizations of the superlattice were calculated by summing the products of the average Born effective charges of the ions with the ionic displacements deviated from the symmetric positions [20,29]. The Born effective charges were calculated from density functional perturbation theory (DFPT) for each ion in both bulk $LuFe_2O_4$ and bulk h-$LuFeO_3$ [30]. For the equivalent ions classified by the Wyckoff positions, the Born effective charges were averaged and used as the corresponding ionic charges in the superlattices.

APPENDIX B: EXPERIMENTAL DESIGN

The single crystalline $LuFe_2O_4$ samples were grown by floating zone method [3]. The TEM work was conducted by a JEOL ARM 200 CF TEM with two correctors at 200 kV in Brookhaven National Laboratory. The convergence angle was 21.2 mrad, and the collection angle was 67–275 mrad for HAADF images. An image filter was slightly applied to reduce the noise.

[1] H. J. Xiang and M.-H. Whangbo, Phys. Rev. Lett. **98**, 246403 (2007).

[2] N. Ikeda, H. Ohsumi, K. Ohwada, K. Ishii, T. Inami, K. Kakurai, Y. Murakami, K. Yoshii, S. Mori, Y. Horibe, and H. Kitô, Nature (London) **436**, 1136 (2005).

[3] M. Angst, R. P. Hermann, A. D. Christianson, M. D. Lumsden, C. Lee, M. -H. Whangbo, J.-W. Kim, P. J. Ryan, S. E. Nagler, W. Tian, R. Jin, B. C. Sales, and D. Mandrus, Phys. Rev. Lett. **101**, 227601 (2008).

[4] J. de Groot, T. Mueller, R. A. Rosenberg, D. J. Keavney, Z. Islam, J.-W. Kim, and M. Angst, Phys. Rev. Lett. **108**, 187601 (2012).

[5] M. Angst, Phys. Status Solidi RRL **7**, 383 (2013).

[6] S. Cheng, C. Xu, S. Deng, M.-G. Han, S. Bao, J. Ma, C. Nan, W. Duan, L. Bellaiche, Y. Zhu, and J. Zhu, Sci. Adv. **4**, eaar4298 (2018).

[7] J. A. Mundy *et al.*, Nature (London) **537**, 523 (2016).

[8] J. M. Rondinelli and C. J. Fennie, Adv. Mater. **24**, 1961 (2012).

[9] F. Jia, S. Xu, G. Zhao, C. Liu, and W. Ren, Phys. Rev. B **101**, 144106 (2020).

[10] W. Wang, J. Zhao, W. Wang, Z. Gai, N. Balke, M. Chi, H. N. Lee, W. Tian, L. Zhu, X. Cheng, D. J. Keavney, J. Yi, T. Z. Ward, P. C. Snijders, H. M. Christen, W. Wu, J. Shen, and X. Xu, Phys. Rev. Lett. **110**, 237601 (2013).

[11] S. M. Disseler, J. A. Borchers, C. M. Brooks, J. A. Mundy, J. A. Moyer, D. A. Hillsberry, E. L. Thies, D. A. Tenne, J. Heron, M. E. Holtz, J. D. Clarkson, G. M. Stiehl, P. Schiffer, D. A. Muller, D. G. Schlom, and W. D. Ratcliff, Phys. Rev. Lett. **114**, 217602 (2015).

[12] P. Suresh, K. Vijaya Laxmi, A. K. Bera, S. M. Yusuf, B. L. Chittari, J. Jung, and P. S. Anil Kumar, Phys. Rev. B **97**, 184419 (2018).

[13] J. C. Leiner, T. Kim, K. Park, J. Oh, T. G. Perring, H. C. Walker, X. Xu, Y. Wang, S.-W. Cheong, and J.-G. Park, Phys. Rev. B **98**, 134412 (2018).

[14] K. Du, B. Gao, Y. Wang, X. Xu, J. Kim, R. Hu, F.-T. Huang, and S.-W. Cheong, npj Quantum Mater. **3**, 33 (2018).

[15] H. Yang, Y. Zhang, Y. Qin, C. Ma, H. Tian, and J. Li, Phys. Stat. Sol. B **247**, 870 (2010).

[16] See Supplemental Material at http://link.aps.org/supplemental/10.1103/PhysRevMaterials.5.094412 for charge ordering and magnetic property of bulk $LuFe_2O_4$, densities of states for bulk $LuFe_2O_4$ and h-$LuFeO_3$, block-by-block polariztions and energies for all the configurations of seven superlattices, typical crystal structures of superlattices, and high-resolution HAADF-STEM images of superlattice-like structures and energy-dispersive X-ray analysis, which includes Refs. [31–33].

[17] R. I. Eglitis and A. I. Popov, J. Saudi Chem. Soc. **22**, 459 (2018).

[18] R. I. Eglitis, J. Purans, J. Gabrusenoks, A. I. Popov, and R. Jia, Crystals **10**, 745 (2020).

[19] Y. Kumagai and N. A. Spaldin, Nat. Comms. **4**, 1540 (2013).

[20] M. Li, Y. Gu, Y. Wang, L.-Q. Chen, and W. Duan, Phys. Rev. B **90**, 054106 (2014).

[21] D. R. Småbråten, Q. N. Meier, S. H. Skjærvø, K. Inzani, D. Meier, and S. M. Selbach, Phys. Rev. Materials **2**, 114405 (2018).

[22] V. Wang, N. Xu, J. C. Liu, G. Tang, and W. T. Geng, Comput. Phys. Commun. **267**, 108033 (2021).

[23] K. Momma and F. Izumi, J. Appl. Crystallogr. **44**, 1272 (2011).

[24] T. Maruyama, Y. Murakami, D. Shindo, N. Abe, and T. Arima, Phys. Rev. B **86**, 054202 (2012).

[25] I. K. Yang, J. Kim, S. H. Lee, S.-W. Cheong, and Y. H. Jeong, Appl. Phys. Lett. **106**, 152902 (2015).

[26] G. Kresse and D. Joubert, Phys. Rev. B **59**, 1758 (1999).

[27] P. E. Blöchl, Phys. Rev. B **50**, 17953 (1994).

[28] J. P. Perdew, A. Ruzsinszky, G. I. Csonka, O. A. Vydrov, G. E. Scuseria, L. A. Constantin, X. Zhou, and K. Burke, Phys. Rev. Lett. **100**, 136406 (2008).

[29] M. Li, J. Li, L.-Q. Chen, B.-L. Gu, and W. Duan, Phys. Rev. B **92**, 115435 (2015).

[30] M. Gajdoš, K. Hummer, G. Kresse, J. Furthmüller, and F. Bechstedt, Phys. Rev. B **73**, 045112 (2006).

[31] Y. Yamada, S. Nohdo, and N. Ikeda, J. Phys. Soc. Jpn. **66**, 3733 (1997).

[32] R. C. Rai, A. Delmont, A. Sprow, B. Cai, and M. L. Nakarmi, Appl. Phys. Lett. **100**, 212904 (2012).

[33] B. S. Holinsworth, D. Mazumdar, C. M. Brooks, J. A. Mundy, H. Das, J. G. Cherian, S. A. Mcgill, C. J. Fennie, D. G. Schlom, and J. L. Musfeldt, Appl. Phys. Lett. **106**, 082902 (2015).